Green Chemistry

LixSiON (x = 2, 4, 6); A Novel Solid Electrolyte System Derived from Agricultural Waste.

Journal:	*Green Chemistry*
Manuscript ID	GC-ART-07-2020-002580.R1
Article Type:	Paper
Date Submitted by the Author:	28-Sep-2020
Complete List of Authors:	Zhang, Xinyu; The University of Michigan, Materials Science and Engineering Center; University of Michigan Temeche, Eleni; The University of Michigan, Materials Science and Engineering; University of Michigan, Material Science and Engineering Laine, Richard; The University of Michigan, Macromolecular Science and Engineering Center

Li_xSiON (x = 2, 4, 6); A Novel Solid Electrolyte System Derived from Agricultural Waste.†

*Xinyu Zhang, Eleni Temeche, Richard M. Laine**
Dept. of Materials Science and Engineering, University of Michigan, Ann Arbor, MI 48109-2136, USA.
E-mail: talsdad@umich.edu

Keywords: Rice hull ash, LiSiON, polymer precursors, solid electrolyte, lithium ion batteries

Abstract

A set of Li_xSiON (x = 2, 4, 6) polymer precursors to a novel solid-state electrolyte system were synthesized starting from rice hull ash (RHA), an agricultural waste, providing a green route towards all solid-state batteries (ASSBs). Silica, ~90 wt. % in RHA, can be catalytically (alkali base) dissolved (20-40 wt %) in hexylene glycol (HG) and distilled directly from the reaction mixture as the spirosilxane [$(C_6H_{14}O_2)_2Si$, SP] at 200 °C. SP can be lithiated using controlled amounts of $LiNH_2$ to produce Li_xSiON oligomers/polymers with MWs up to ~1.5 kDa as characterized by FTIR, MALDI-ToF, multinuclear NMR, TGA-DTA, XRD, XPS, SEM and EDX. XPS analyses show that Li contents depend solely on added $LiNH_2$ but found N contents are only ≤1 at. %. NH_2 likely is removed as NH_3 during sample preparation (vacuum/overnight). In contrast, MALDI indicates N contents of ~5-30 at. % N with shorter drying times (vacuum/minutes). ^7Li NMR positive chemical shifts suggest that precursor bound Li^+ ions dissociate easily, beneficial for electrochemical applications. The ^7Li shifts correlate to Li contents as well as Li^+ conductivities. ^1H, ^{13}C and ^{29}Si NMRs of the Li_6SiON precursor show fluxional behavior implying high Li^+ mobility. Dense microstructures are observed for Li_4SiON and Li_6SiON pellets heated to 200 °C/2 h/N_2 by SEM. Impedance studies suggest that ionic conductivities increase with Li content; the Li_6SiON precursor offers the highest ambient conductivity of 8.5×10^{-6} S cm^{-1} after heating to 200 °C/2 h/N_2.

†This paper is dedicated to the memory of Prof. Dr. Dr. Andreas Hintennach, deceased May 10, 2020, a friend and mentor.

1. Introduction

To reduce the consumption of traditional energy sources, i.e., fossil fuels, and emission of greenhouse gases, researchers have long sought to replace combustion-based energy technologies. Electrochemical energy storage/conversion systems, including lithium-ion batteries (LIBs), have become subjects of great interest.[1–3] Although LIBs are now used intensely in applications ranging from simple replacements for traditional batteries in toys, medical devices, portable electronics and are instrumental in the commercialization of electric vehicles; the use of organic solvent based liquid electrolytes with inadequate electrochemical and thermal stabilities introduces inherent safety risks and restrains operating temperatures.[4–7] Non-flammable, solid-state electrolytes offer an escape from such problems offering potential for both wider operating temperatures coincident with higher energy-densities.[4–6,8] The potential to formulate solid-state electrolytes from agricultural waste (e.g. rice hull ash, RHA) therefore offers two exciting opportunities. One is to valorize the waste of a commodity product (rice hull ash) and the potential to coincidentally reduce the carbon footprint of extensively used battery materials. This then is the motivation for work reported here.

Li^+-containing oxynitride amorphous thin films are promising materials for electrochemical applications as solid electrolytes due to their high ionic conductivity, mechanical stability and chemical durability. Most studies focus on LiPON thin films as suggested by the extensive literature on this topic.[9–35] There are a few reports on borate analogs, lithium boron oxynitrides (LiBON).[36–39] However, the ionic conductivity (at ambient) for LiBON (10^{-8} S cm^{-1}) is much lower than LiPON (10^{-6} S cm^{-1}).[9–12] Studies on other Li-containing oxynitrides are also reported including lithium sulfur oxynitride (LiSON) with ambient conductivities of 10^{-6}-10^{-5} S cm^{-1},[40,41] and lithium vanadium oxynitride (LiVON) with conductivities of 10^{-4}-10^{-5} S cm^{-1} at 330 °C.[42,43]

A number of research groups have explored MSiON (M = Li, Na) glass-ceramics with respect to their crystallization and bonding arrangements,[44–48] mechanical properties,[44,47] chemical durability and conductivities.[49,50] Typically, such glasses are prepared by melt mixing Li_2O or Na_2O, SiO_2 and Si_3N_4 at 1400-1500 °C/1-3 h in BN crucibles under N_2.[45,46,48–50] The conductivity for MSiON is attributed to alkali ion transport, which increases with increasing N content.[49,50] The literature explanation for this behavior suggests that Si-N bonds are more covalent (less ionic) than Si-O bonds, the electrostatic force exerted on alkali ions decreases upon nitridation resulting in

reduced activation energy.[44–50] A similar N for O effect is found for LiPON glasses.[13–18] However, the ambient conductivities of M-Si-O-N glasses remain at 10^{-8}-10^{-7} S cm^{-1}.

A doctoral thesis by Jarkaneh[43] describes novel Li^+ oxynitride conductors including $Li_{3+x}PO_{4-x}N_x$, $Li_{3+x}VO_{4-x}N_x$, $Li_{2+y}ZnSiO_{4-y}N_y$ and $Li_{2+y}MgSiO_{4-y}N_y$ solid solutions. N-doping of all compositions generates a γ-phase, except in Li_3VO_4 which generates a β-phase. The γ-phase structures are typical for Li^+ superionic conductors (LISICON), where cations are tetrahedrally coordinated.

As shown in Table **S1**, N-doping improves conductivities by up to two orders of magnitude in N-doped $Li_3(P,V)O_4$ and 4-6 orders in N-doped $Li_2(Zn,Mg)SiO_4$. The activation energy decreases by about 0.3 eV in N-doped $Li_3(P,V)O_4$ and 0.6-0.7 eV in N-doped $Li_2(Zn,Mg)SiO_4$. Higher ionic conductivities and lower activation energies in N-doped samples are attributed to higher numbers of interstitial Li^+ created as a result of substitution of N for O. Therefore, it is reasonable to envision that N-doping of other γ-structured materials, including Li_4SiO_4, can be expected to improve ionic conductivity.

Indeed, studies show that Li_4SiO_4 may offer utility as a solid electrolyte. Wu *et al*.[51,52] synthesized Li_4SiO_4 powders (particle sizes ≈ 100 nm) via sol-gel processing using SiO_2 (aerosil) and $LiOH{\cdot}H_2O$ as the starting materials and citric acid ($C_6H_8O_7{\cdot}H_2O$) as the chelating agent. Li_4SiO_4 pellets (diameter = 10 mm, thickness = 2 mm) sintered at 1000 °C/4 h exhibited bulk conductivities of ~10^{-3} S cm^{-1} at 400 °C. Similarly, Adnan *et al*.[53] prepared Li_4SiO_4 powders by sol-gel, then pelletized and sintered at 600-750 °C/4 h finding a bulk conductivity of ~3×10^{-6} S cm^{-1} at ambient, suggesting potential use as LISICON structured solid electrolytes for low-temperature applications.

Furthermore, various studies have described Li_4SiO_4-based solid electrolytes, including the binary and ternary systems: Li_4SiO_4-Li_3XO_4 (X = V, As, P, *etc*.),[54–59] and Li_2S-SiS_2-Li_4SiO_4.[60–64] For the binary system, compositions with 40-60 mol. % Li_4SiO_4 typically give the highest ionic conductivities of ~10^{-6} S cm^{-1} at 20 °C.[55,57–59] For the ternary system, the composition (1-z)[$0.6Li_2S$-$0.4SiS_2$]-zLi_4SiO_4 (z = 0-10 mol. %) exhibits a room temperature conductivity of 10^{-4}-10^{-3} S cm^{-1}.[60–63]

The above studies suggest that Li_4SiO_4 is a reasonable candidate for solid electrolyte applications. However, to the best of our knowledge, there have been no reports on N-doped Li_4SiO_4 (or Li_xSiON) as solid electrolytes. Given our previous success in developing polymer

precursor derived Li_xPON-like electrolytes,[65–67] we present here a novel and green approach to Li_xSiON oligomer/polymer precursors (x = Li/Si mole ratio).

Recently, we reported processing "green" hybrid Li^+ capacitors (LICs) electrodes using the plentiful agricultural waste, RHA, as the starting material.[68] The basis for this report was the use of silica depleted RHA (SDRHA, ≈ 65 wt. % SiO_2, 35 wt. % C); a carbon/silica nanocomposite. This nanocomposite derives from SiO_2 extraction from RHA by simple distillation of the spirosiloxane [$(C_6H_{14}O_2)_2Si$, SP] at 200 °C, as illustrated in reaction (1):

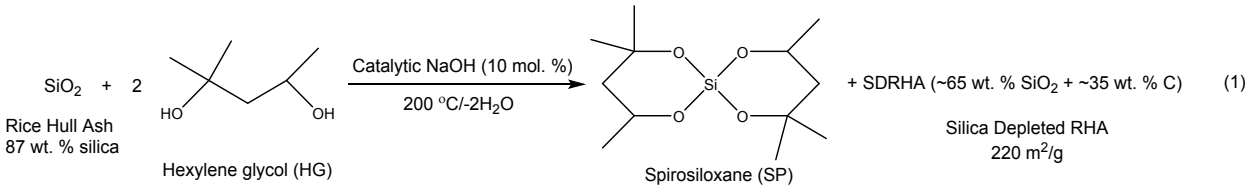

We report here that this spirosiloxane "byproduct" provides the starting point for a series of Li^+ conducting polymer precursors on reaction with $LiNH_2$, generically illustrated by reaction (2). Such a synthetic approach provides environmental advantages including green source, low cost, low temperature, low energy consumption, emission-free, and scalable features.

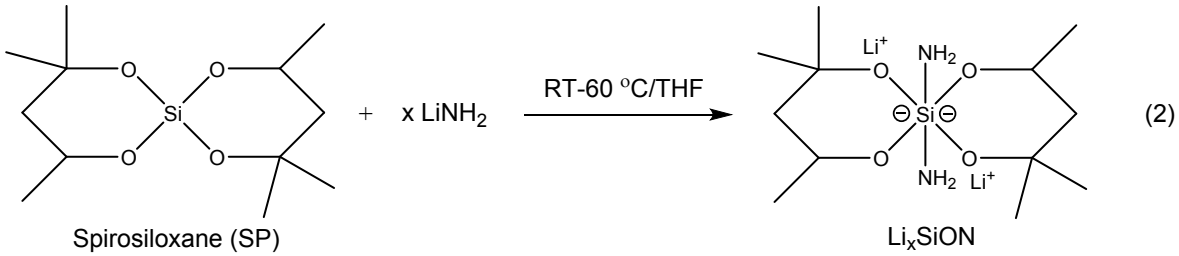

2. Experimental section

2.1. Materials

RHA was provided by Wadham Energy LP (Williams, CA); it was milled in dilute hydrochloric acid (HCl) to remove impurities prior to use.[68,69] The solvent and reactants, 2-Methyl-2,4-pentanediol (hexylene glycol, HG) and lithium amide ($LiNH_2$) were purchased from Acros Organics. Sodium hydroxide (NaOH), HCl and tetrahydrofuran (THF) were purchased from Sigma-Aldrich. Hexane was purchased from Fisher Chemical, and ethanol was provided by Decon Labs, Inc. THF was distilled over sodium benzophenone ketyl prior to use. All other chemicals were used as received.

2.2. Synthesis of spirosiloxane

Silica from RHA can be reacted with HG using catalytic base forming SP at 200 °C,[70,71] which distills directly out of the reaction mixture per equation (1).

Typical spirosiloxane synthesis: to a dry 500 mL round-bottom flask are added 300 mL HG (excess amount) and NaOH (3.0 g, 75 mmol). The solution is heated to 200 ℃/3 h with stirring to remove water, then dried RHA (~50 g, ~90 wt. % silica content) is added. After 100 mL HG distills off, another 100 mL HG is added until 500 mL HG has reacted and/or distilled out as a mixture of SP, H_2O and HG during silica depolymerization.

The distilled mixture of SP, H_2O and HG (500 mL) is washed with hexane (500 mL) and water (3 × 250 mL). HG is soluble in water, but SP is not. Then the hexane layer (containing SP) is dried over magnesium sulfate and collected. In the final step, the hexane is removed on a rotary evaporator to yield 37 g of the SP product (~70 % yield). The SP can be further purified by redistillation. The product is dried at 60 °C/12 h/vacuum.

The remaining SDRHA is filtered off. Figure **S1** compares the TGA-DTAs of RHA before and after reaction, *i.e.*, RHA and SDRHA, which show silica contents of 88 and 64 wt. % respectively (ceramic yield or CY at 800 °C), suggesting ~27 wt. % silica dissolution.

2.3. Syntheses of Li_xSiON precursors

Li_xSiON precursors are synthesized by reacting SP with $LiNH_2$ (mole ratio of $LiNH_2$/SP = x), as suggested in equation (2). In theory, one SP molecule can be envisioned to offer two coordination sites for $LiNH_2$ (Li_2SiON),[72] but below our studies suggest that excess $LiNH_2$ can react with SP forming Li_4SiON and Li_6SiON precursors likely by partial displacement of one or more Si-O bonds.

Example of Li_6SiON synthesis: in a 200 mL round bottom Schlenk flask equipped with a reflux condenser, SP (3.9 g, 15.0 mmol) and $LiNH_2$ (2.2 g, 95.8 mmol) are added to ~80 mL distilled THF under N_2. The reaction is kept running at 60 °C/2 weeks (w)/N_2. Initially, the reaction is a cloudy white mixture that turns darker over time. After running at 60 °C/2 w, the reaction mixture becomes a brown solution (Figure **S2**).

To obtain the yield, the reaction mixture is allowed to settle for 1 h, a small sample (5 mL) is taken from the top of the mixture to a 25 mL Schlenk flask, and vacuum dried at 60 °C/1 h. The product is a 0.37 g orange solid indicating a total yield for the solution of ~6 g; slightly lower than the mass sum of the starting materials (6.1 g) suggesting the product is almost fully soluble and stable in THF. Table **1** records the $LiNH_2$ quantities used for different precursors. Figure **S3** shows optical images of representative Li_xSiON precursor powders dried at 60 °C/1 h/vacuum and pellets pelletized hydraulically at 10 ksi/20 sec with a 13 mm diameter die.

Table 1. Syntheses of Li_xSiON precursors.

Precursor	$LiNH_2$/SP[a]	Appearance[b]
Li_2SiON	2.1-2.2	Orange/light-brown solution
Li_4SiON	4.2-4.4	Orange/light-brown solution
Li_6SiON	6.4-6.6	Brown solution

[a]Typically, a 5-10 mol. % excess $LiNH_2$ is added. [b]The appearances of precursor THF solutions (Figure **S2**).

3. Results and discussion

Our objectives in this work were first to carefully verify that the prepared precursors contain nitrogen and form oligomers as the first step in exploring their utility as LiSiON precursors. Once having demonstrated well-defined compositions, the next step was to explore their properties as electrolytes. For clarity and simplicity, the precursors are simply labeled as Li_xSiON (x = 2, 4, 6) rather than including a complete chemical formula for reasons that become apparent below.

The apparent structures and chemical compositions of Li_xSiON precursors were analyzed using FTIR, matrix-assisted laser desorption/ionization (MALDI-ToF), multi-nuclear NMR, TGA-DTA, XRD, X-ray photoelectron spectroscopy (XPS), scanning electron microscopy (SEM) and energy-dispersive X-ray spectroscopy (EDX). The results of these analyses are presented just below followed by electrochemical impedance spectroscopy (EIS) characterization.

3.1. Characterization of Li_xSiON precursors

Figure **1a** shows representative FTIRs of Li_xSiON (dried at 60 °C/1 h/vacuum) compared to SP. All precursors show similar SP peaks peaks; in addition, the broad peak at ~3400 cm^{-1} is ascribed to νN-H, with N-H overtones at ~1600 cm^{-1}. The Li_4SiON and Li_6SiON precursors exhibit a small νN-H peak at ~3600 cm^{-1} evident of residual, unreacted $LiNH_2$ (Figure **S4**) as excess $LiNH_2$ was used to synthesize both Li_4SiON and Li_6SiON precursors. Li_xSiON precursors dried at temperatures ≤100 °C show similar FTIRs as illustrated by the **1b** FTIRs of Li_6SiON dried at RT-100 °C/vacuum. Likewise, as discussed below, very similar XRD patterns are also observed for precursors dried at low temperatures (≤100 °C).

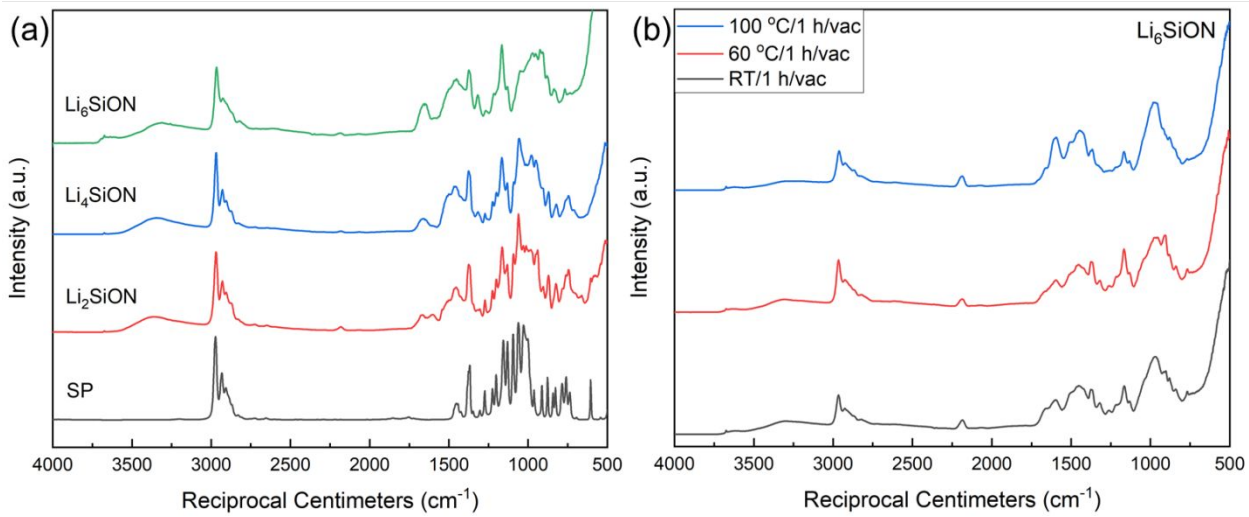

Figure 1. FTIRs of **a**. Li_xSiON precursors (60 °C/1 h/vacuum) and SP (60 °C/12 h/vacuum), **b**. Li_6SiON dried at RT, 60° and 100 °C/1 h/vacuum.

Precursor molecular weights (MWs) as well as possible compositions were analyzed using both positive- and negative-ion MALDIs, as done previously for Li_xPON and Li_xSiPON precursors.[65,66] The ion source in the negative-ion mode comes from the precursor itself which loses Li^+; for the positive-ion mode, the ion source is Ag^+ from $AgNO_3$ and there is no loss of Li^+. With the assistance of a Python program (see SI), calculations based on MALDI provide insights into the materials' possible compositions and structures.

Figure **2** shows positive-ion mode MALDIs of Li_xSiON precursors and possible compositions of selected peaks. Negative-ion mode MALDIs are given in Figure **S5**; the complete composition calculations are listed in Table **S2**. Table **2** records calculated properties of Li_xSiON precursors derived from MALDI peaks and their intensities.

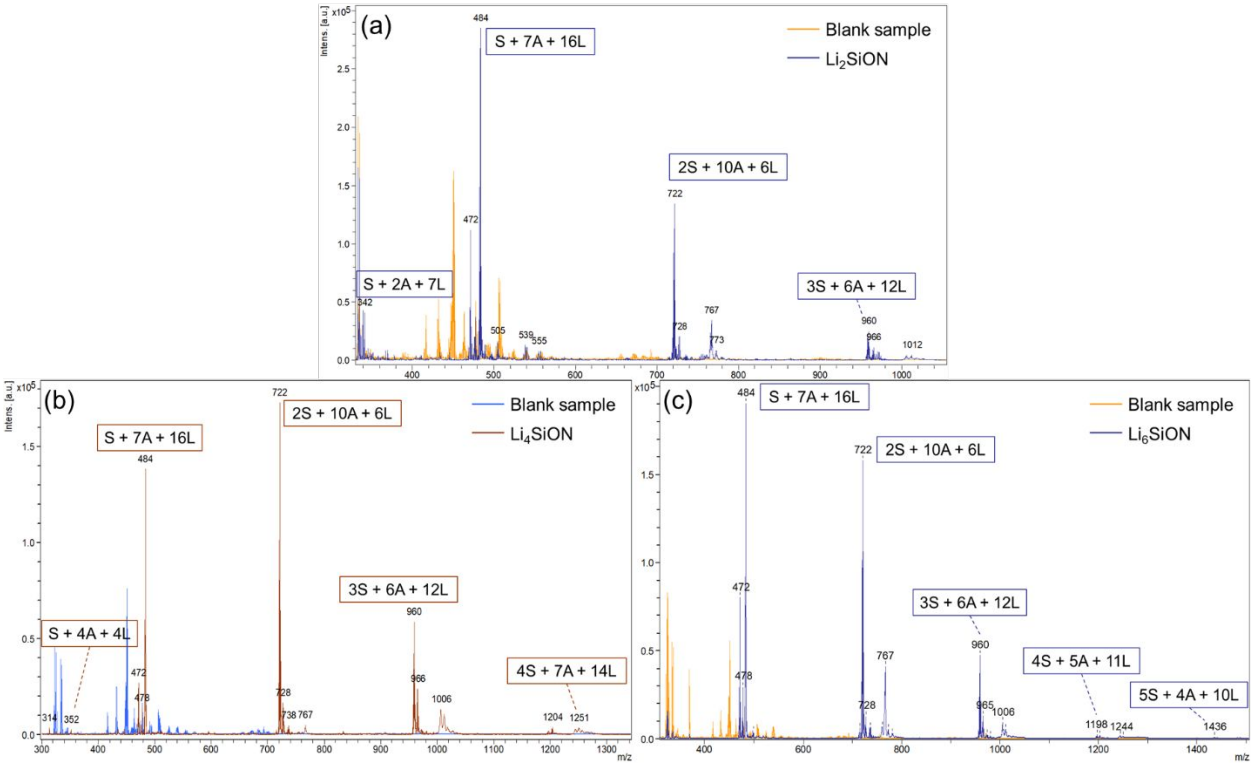

Figure 2. Positive-ion mode MALDIs of blank vs Li_xSiON precursors, **a**. Li_2SiON, **b**. Li_4SiON and **c**. Li_6SiON, and possible compositions of selected peaks. S = SP, A = $-NH_2$, L = Li^+.

In general, the Li_xSiON precursors show similar peaks with each peak consisting of different combinations of SP, $-NH_2$ and Li^+. With higher Li content, the maximum MW (highest m/z) increases; all precursors formed oligomers with SP = 3-5 (Table **2**). Composition calculations (Figure **2** and Table **S2**) suggest that there are typically 5-10 $-NH_2$ groups and 8-13 Li^+ in each precursor structure with only 1-5 SP units, which is much higher than available sites for $LiNH_2$

(two for each SP, see Scheme **2**). One possible explanation is that some Li^+ containing species exist as clusters in addition to those that interact with SP. It is also possible that ring-opening leads to the formation of more Si-NH bonds and Li-O-HG bonds, NMR data below do not support such conclusions but in fact also do not disprove the possibility.

A similar pattern is observed for both ion modes: precursors show peaks in separate groups, the difference between every two peaks in each group is typically 7 or 14 Da, which corresponds to one or two Li^+ (7 Da). In some cases, the distance of two peaks is 15-16 Da, which fits better with $-NH_2$ (16 Da). It is likely that each group of peaks corresponds to a certain structure, and each peak in that group corresponds to different numbers of Li^+ and $-NH_2$. The composition calculations listed in Table **S2** also indicates such pattern.

Additionally, similar or the same peaks are observed in both positive/negative-ion modes, but the start/end peaks of each group in the positive-ion mode generally shift higher (integer × 7 m/z = different numbers of Li^+) as there is no loss of Li^+.

Table 2. Properties of Li_xSiON precursors derived from MALDI.

Precursor	Max. MW (m/z)[a]	Max. monomer units[b]	N At. %[c]	Li At. %[c]
Li_2SiON	1012 (P) 946 (N)	3 (P) 3 (N)	7.7 ± 3.0 (w. H) 17.4 ± 6.7 (wo. H)	8.3 ± 4.6 (w. H) 18.2 ± 8.7 (wo. H)
Li_4SiON	1251 (P) 1002 (N)	4 (P) 3 (N)	8.5 ± 2.8 (w. H) 18.9 ± 6.2 (wo. H)	9.7 ± 5.1 (w. H) 20.9 ± 9.7 (wo. H)
Li_6SiON	1436 (P) 1196 (N)	5 (P) 4 (N)	8.4 ± 2.9 (w. H) 18.6 ± 6.5 (wo. H)	9.2 ± 4.7 (w. H) 21.1 ± 8.6 (wo. H)

[a]Maximum molecular weights. P = positive-ion mode, N = negative-ion mode. [b]Maximum monomer units = maximum number of SP by calculation. [c]Calculated N/Li atomic percentages. "w. H": including H as part of the calculation; "wo. H" excluding H, providing comparison to XPS studies below.

Atomic percentages (At. %) of N and Li calculated from possible compositions (Table **S2**) are also given in Table **2**. Since the composition calculation derived from MALDI gives mathematical combinations and multiple possible results are generated for each peak; for convenience, only one is chosen that may not reflect the true structure. Therefore, the At. % calculated from MALDI is meant solely to give a qualitative idea of N contents. As discussed below, XPS and EDX studies were performed to deduce the elemental At. % makeup of the Li_xSiON precursors.

The chemical environments and structures for Li_xSiON precursors, were further elucidated using NMR. Dried Li_xSiON powders (0.05 g, RT/1 h/vacuum) were dissolved in 1 mL $CDCl_3$.

Figure **S6** compares the ^1H NMRs of the Li_xSiON precursors (RT/1 h/vacuum), THF and SP. All Li_xSiON precursors show peaks at 3.7 and 1.8 ppm in addition to SP peaks, which are ascribed

to residual THF. Unlike Li_4SiON and Li_2SiON precursors, Li_6SiON shows no original SP peaks but a broad peak at 1-1.5 ppm (-C**H**$_3$/C**H**$_2$) indicating fluxional behavior.[73,74]

To eliminate residual THF, Li_xSiON precursors were further dried at 60 °C/24 h/vacuum in a vacuum oven. The dried solids (0.05 g each) were added to 1 mL $CDCl_3$, respectively. All formed suspensions after stirring overnight/RT, suggesting reduced solubility after prolonged drying.

Figure **3** compares the ^{1}H NMRs of the Li_xSiON precursors (60 °C/24 h/vacuum) and SP, no THF peaks (3.7 and 1.8 ppm) are observed. Similar to precursors dried at RT/1 h/vacuum (Figure **S6**), Li_6SiON (60 °C/24 h/vacuum) shows only a small and broad -C**H**$_3$/C**H**$_2$ peak at 1.2-1.3 ppm, suggesting fluxional behavior.

Both Li_4SiON and Li_2SiON precursors show a peak at 4.2 ppm, likely the -C**H**O group from SP that shifts due to interaction with Li^+, suggesting Li^+ interacts more directly with O lone electron pairs from SP. The same -C**H**$_3$ peaks from SP are observed in Li_4SiON and Li_2SiON precursors, but the intensity is reduced for Li_4SiON, suggesting there may be partial fluxional behavior for the Li_4SiON precursor.

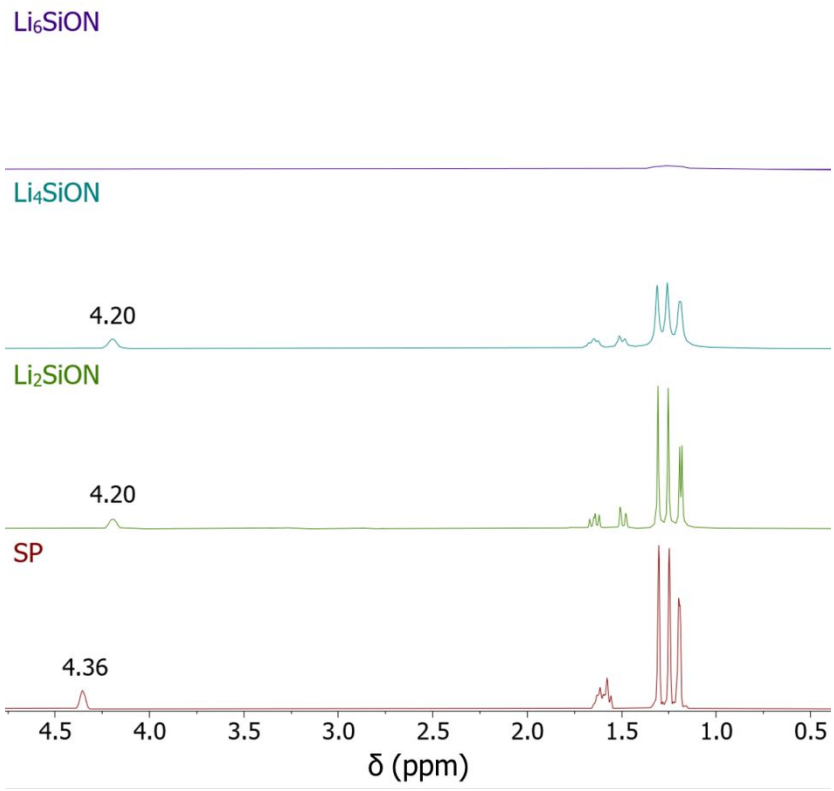

Figure 3. ^{1}H NMRs of Li_xSiON precursors (60 °C/24 h/vacuum) and SP.

Similarly, ^{13}C NMRs of the Li_xSiON precursors dried at RT/1 h/vacuum exhibit THF peaks at 68.1 and 25.7 ppm (Figure **S7**), but no THF peaks are observed for Li_xSiON precursors dried at 60 °C/24 h/vacuum (Figure **4**). Both Li_4SiON and Li_2SiON (60 °C/24 h/vacuum) show small SP peaks that shift due to interaction with Li^+, and the -**C**O and -**C**HO show higher $\Delta\delta_C$ (qualitative, blue dash lines in Figure **4**) than -**C**H_2 and -**C**H_3 peaks, suggesting Li^+ likely interacts with the O from SP, in agreement with the ^1H NMR.

The disappearance of SP peaks for the Li_6SiON precursor (Figures **4** and **S7**) again reflects fluxional behavior pointing to rapid exchange of Li^+ in associated clusters. Lee *et al*.[75] studied exchange dynamics in Li^+ liquid electrolytes of 1.0 M $LiPF_6$ in DEC and PC/DMC (1:1 vol.). Ultrafast fluxional behavior of Li^+-carbonate complexes is observed (electrostatic interactions forming and breaking in picoseconds) as proven by coherent 2-D infrared spectroscopy, suggesting macroscopic Li^+ transport may be related to microscopic fluctuation of solvation. We can suggest that fast chemical exchange dynamics will also play an important role in solvation and de-solvation of Li^+ in solid polymer electrolytes.

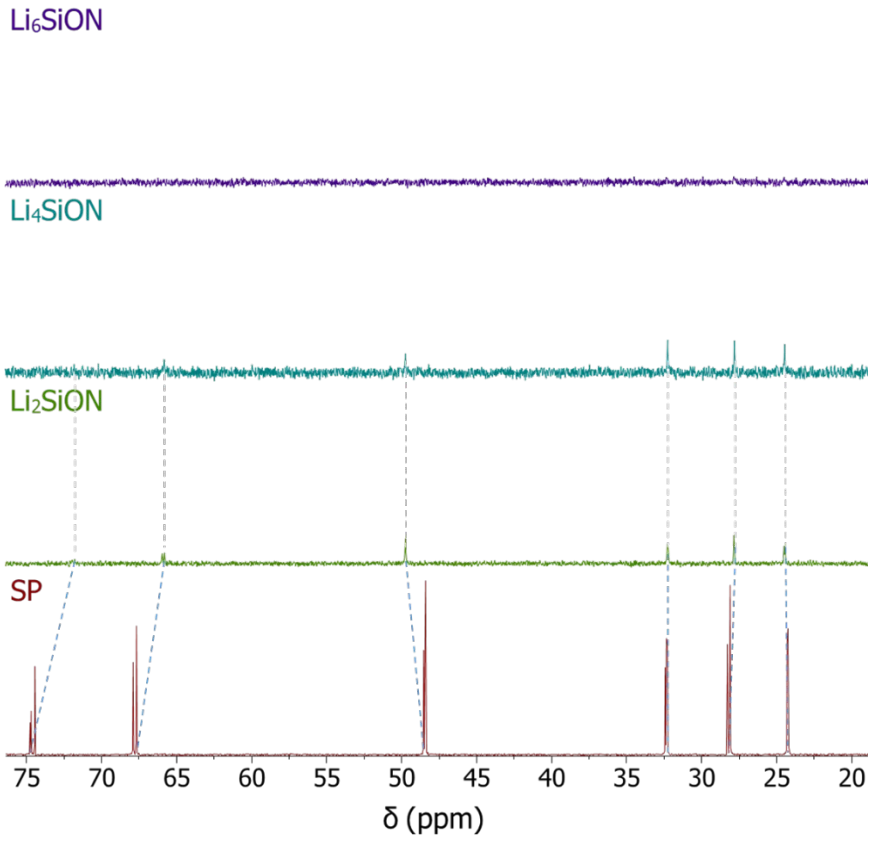

Figure 4. ^{13}C NMRs of Li_xSiON precursors (60 °C/24 h/vacuum) and SP.

Figure **5** compares the ^{7}Li NMRs of Li_xSiON precursors (RT/1 h/vacuum), the δ_{Li} shifts downfield with increasing Li content, especially for the Li_6SiON precursor suggesting Li^+ ions are well solvated. The excess Li^+ likely forms clusters in agreement with work of See *et al*.[76] where δ_{Li} shifts to higher frequencies as Li^+ concentration increases (LiTFSI in DOL/DME), as also found in our previous studies on Li_xPON-like polymer precursors.[65] These results suggest the downfield shift is due to deshielding of Li^+ (reduced electron density around Li^+), i.e., increased numbers of Li^+ interacting with one SP molecule (coordination numbers change).

However, broad ^{7}Li bands with low intensities centered at ~0 ppm are observed for Li_xSiON precursors dried at 60 °C/24 h/vacuum due to low solubility (Figure **S8**), suggesting that THF aids in dissolution of Li^+.

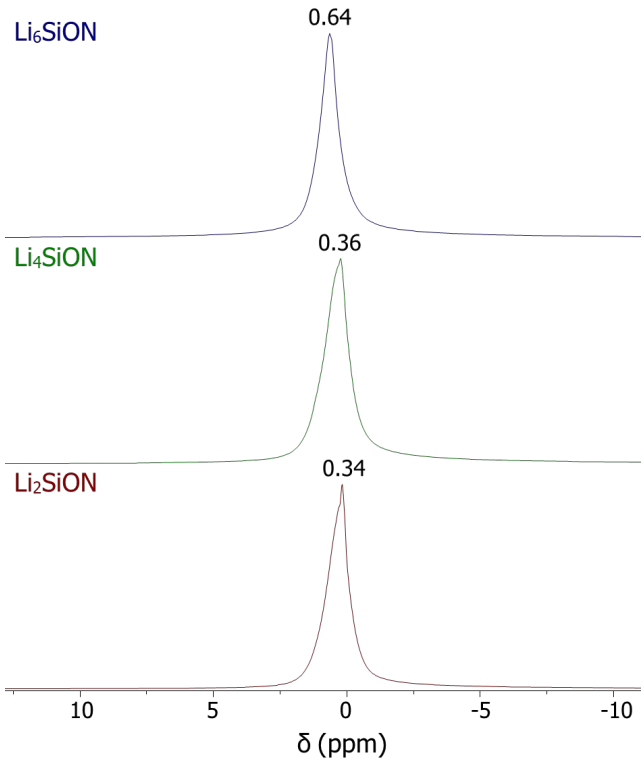

Figure 5. ^{7}Li NMRs of Li_xSiON precursors (RT/1 h/vacuum).

^{29}Si NMRs of Li_xSiON precursors and SP are presented in Figure **S9**. For precursors dried at RT/1 h/vacuum (Figure **S9a**), similar to ^{1}H and ^{13}C studies, no SP peaks were found for the Li_6SiON precursor, while Li_2SiON and Li_4SiON precursors show the same δ_{Si} at -81.3 ppm as SP,

suggesting no chemical environment change on the O-Si-O bonds for Li_2SiON and Li_4SiON precursors, but fluxional behavior for the Li_6SiON precursor.

However, no ^{29}Si signals are observed for Li_xSiON precursors dried at 60 °C/24 h/vacuum (Figure **S9b**), likely due to reduced solubility, in agreement with ^{7}Li NMR above.

The thermal stability of Li_xSiON precursors were investigated by TGA-DTA studies. Figure **6** compares representative TGA-DTAs (800 °C/10 °C min^{-1}/N_2) of Li_xSiON precursors (dried at 60 °C/1 h/vacuum). All precursors typically show 5 % mass loss temperatures ($T_{5\%}$) >100 °C; the major mass loss (from ~100 °C to ~300°-450 °C) is associated with evaporation and/or decomposition of organics. Additionally, the Li_6SiON precursor exhibits a second mass loss at ~650 °C, associated with excess $LiNH_2$ decomposition.[77] Overall, the CYs (800 °C) of Li_xSiON precursors are Li_6SiON > Li_4SiON > Li_2SiON in ~10 wt. % increments (Figure **6**) correlated with MWs (Figure **2** and Table **2**) and Li contents.

Unlike the Li_xSiON precursors, SP evaporates/distills fully at ~100°-200 °C (Figure **S10**) due to its high vapor pressure. Consequently, added $LiNH_2$ promotes formation of oligomers/polymers with higher MWs and stable polymer precursors and eventually ceramics form at higher temperatures as demonstrated below.

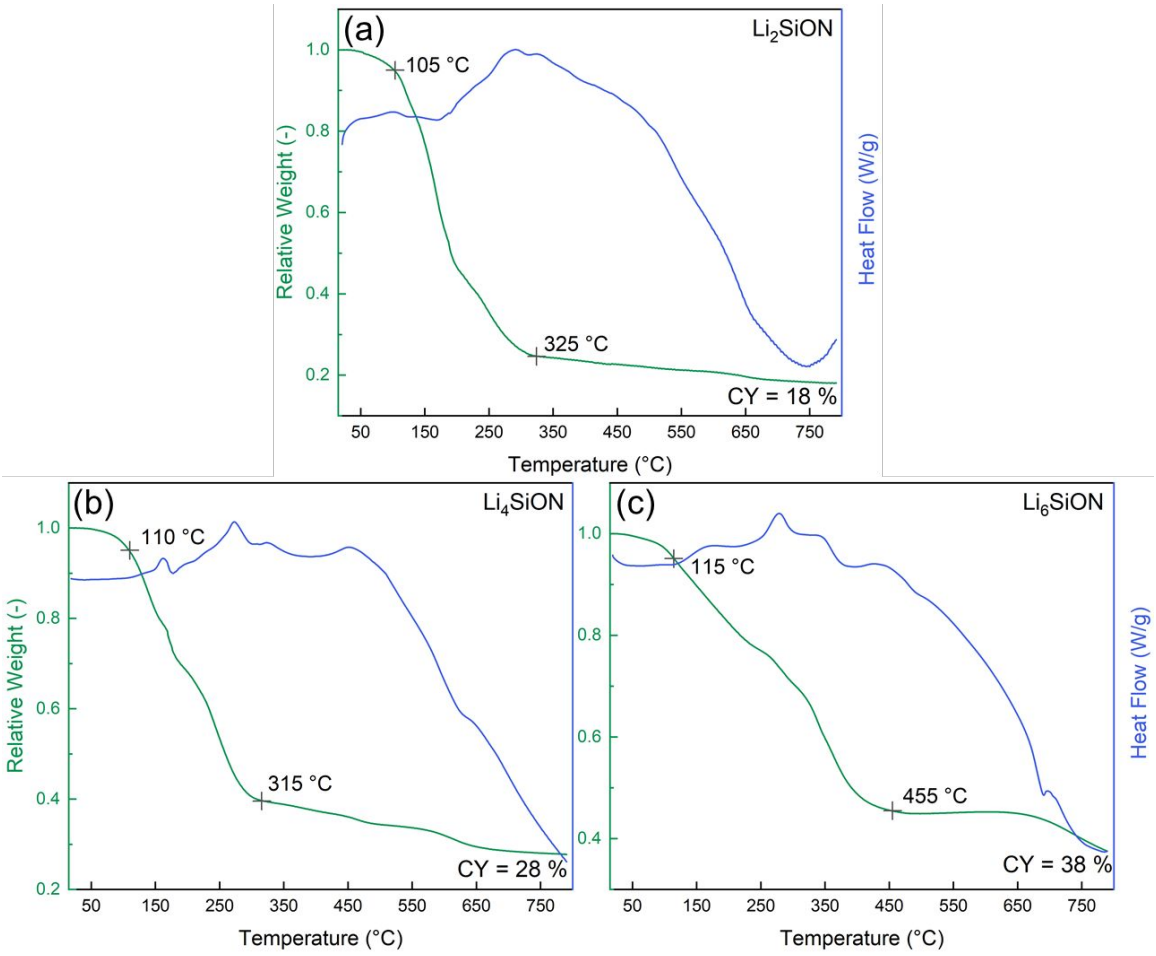

Figure 6. TGA-DTAs (800 °C/10 °C min^{-1}/N_2) of **a**. Li_2SiON, **b**. Li_4SiON and **c**. Li_6SiON precursors dried at 60 °C/1 h/vacuum.

Figure **S11a** compares the XRDs of Li_xSiON (dried at 60 °C/1 h/vacuum) and SP. SP exhibits various crystalline peaks that are indexed to space group 10: P2/m by Expo2014, while the Li_xSiON precursors show a broad peak at ~20° 2θ suggesting amorphous materials, indicating that SP reacts fully. As mentioned above, when dried at temperatures ≤100 °C, Li_xSiON precursors show similar XRD patterns, see Figure **S11b** comparing XRDs of Li_6SiON dried at RT-100 °C/vacuum as an example. It's noteworthy that there is a small peak at 33° 2θ in the XRD corresponding to $Li(OH)(H_2O)$, likely due to brief interactions with atmospheric moisture during sample preparation, but the intensity is very low.

To study XRDs of Li_xSiON precursors heated to higher temperatures (>100 °C), dried polymer precursor powders (60 °C/24 h/vacuum, 0.1-0.2 g) were compacted into pellets using a 13 mm

diameter die at 10 ksi/RT (Figure **S3**). The resulting pellets were heated between Al_2O_3 disks to 100°-400 °C/2 h at 1 °C min^{-1} under 120 ml min^{-1} N_2 flow.

Figure **7** presents XRD patterns of Li_xSiON pellets heated to 100°-400 °C/2 h/N_2. XRD of Li_2SiON pellet (Figure **7a**) heated to 100 °C exhibits small peaks at ~20° and 30° 2θ, corresponding to $LiSi_2N_3$ (PDF-01-086-6830) with space group Cmc21. The pellet also exhibits a large broad peak from ~30° to 40° 2θ with a central and shoulder peaks at 35° and 38° 2θ associated with an amorphous phase. The small peak ~30° 2θ disappears when the Li_2SiON pellet is heated to 200°-300 °C. The broad peak seems to shift to lower diffraction angles (20°-30° 2θ) when the pellet is heated to 400 °C.

Figure **7b** shows that Li_4SiON pellets presents a broad peak similar to Li_2SiON after heating to 100 °C. No apparent sharp peaks appear on heating to 200°-300 °C confirming the absence of any ordered crystalline structure. At 400 °C, the amorphous peak shifts to lower diffraction angles with a shoulder peak at ~32° 2θ, suggesting that the lattice is expanding. This might be ascribed to nitrogen loss which results in a change in composition and structure.

The XRD of Li_6SiON pellets (Figure **7c**) at 100 °C is dominated by a broad peak corresponding to a poorly crystallized material, indicating an amorphous nature. The sharp peak at 35° 2θ can be indexed to partially crystalline Li_4SiO_4 (PDF-01-084-7600) after heating to 200 °C. The single peak at ~22° 2θ starts to split into doublets when the Li_6SiON pellet is heated above 300 °C. The doublets at ~30° 2θ for the pellet heated to 400 °C corresponds to Li_2CO_3 (PDF-04-0101-7186). Since, Li_6SiON precursor contains a slight $LiNH_2$ component, it is quite likely to form Li_2CO_3 during the decomposition process, which will generate CO_2.

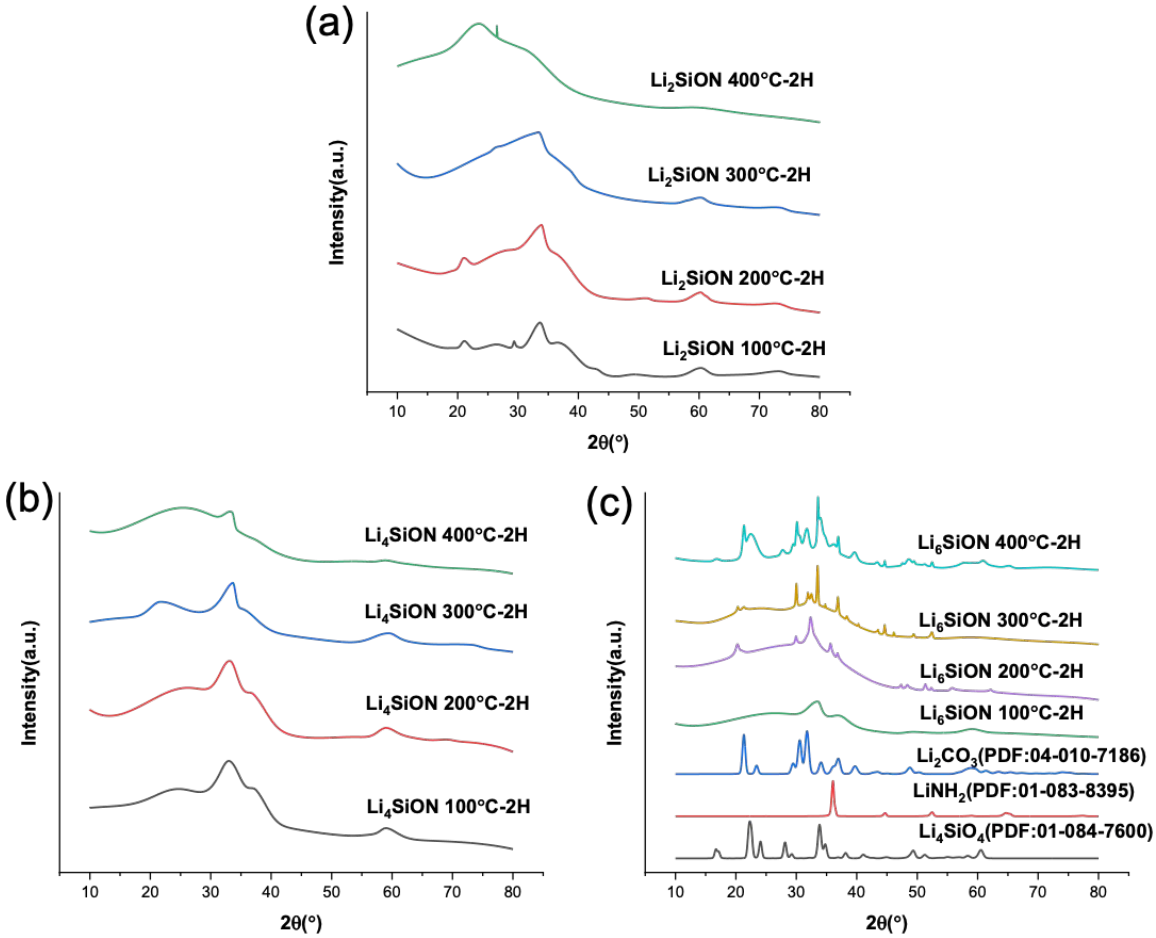

Figure 7. XRDs of **a**. Li_2SiON, **b**. Li_4SiON, **c**. Li_6SiON pellets heated to 100°-400 °C/2 h/ N_2.

The amorphous nature of the Li_xSiON precursors ≤100 °C by XRD fails to reveal elemental compositions of as synthesized materials. Hence, Li_xSiON precursors (dried at ≤100 °C, powders) were characterized by XPS. For each sample, a wide-scan survey was done on three separate points for better accuracy. As shown in Figure **8**, all precursors show peaks for O, C and Li, small amounts of N and Si, and little difference is observed at different drying temperatures. SP, on the other hand, only shows peaks for O, C, and Si with higher intensity (Figure **S12**).

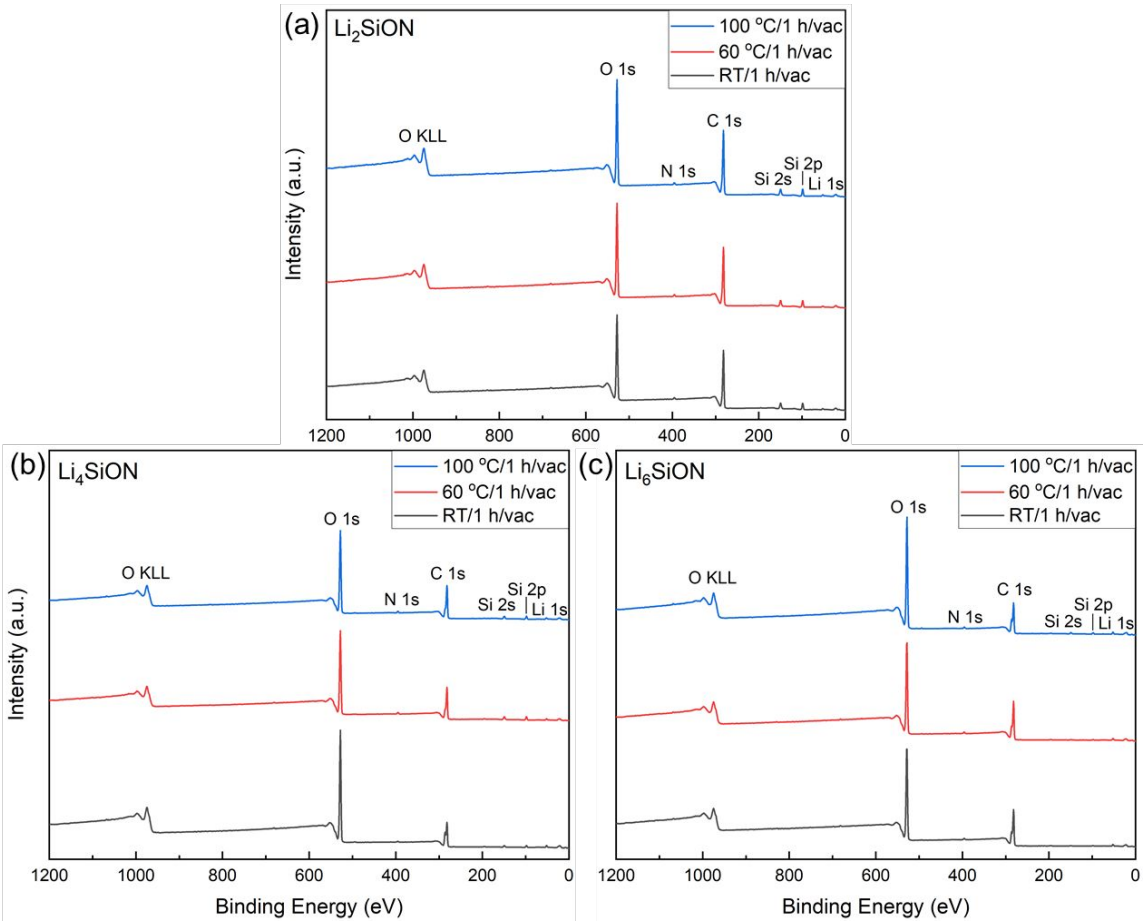

Figure 8. Wide-scan survey XPS spectra of Li_2SiON (a), Li_4SiON (b) and Li_6SiON (c) precursors dried at RT, 60° and 100 °C/1 h/vacuum respectively.

Table **3** summarizes the average At. % for Li_xSiON precursors dried at different temperatures compared to SP. In general, Li_xSiON precursors show lower C and Si contents compared to SP as expected, but the O content increases which may be LiOH and/or Li_2CO_3 formed due to brief exposure in air.

The At. % for all Li_xSiON precursors stay nearly the same after drying at different temperatures under vacuum. The Li content increases with the amount of added $LiNH_2$ as expected, but the increase from Li_4SiON to Li_6SiON is smaller than the increase from Li_2SiON to Li_4SiON, suggesting that Li content saturation is likely reached for the Li_6SiON precursor. The fluxional nature of this one precursor belies the large excess of $LiNH_2$ originally added and strongly suggests novel chemistry for this system since, we originally assumed that only two amide groups might be accommodated based on equation (2). Unfortunately, this same fluxional nature means that NMR characterization was not possible at least at ambient.

For Li_2SiON and Li_4SiON precursors, C and Si contents decrease with increasing Li content, but the O content shows the opposite trend. As mentioned above, this is likely a result of LiOH and/or Li_2CO_3 forming, and a higher Li content leads to a higher O content.

Table 3. Average atomic percentage (At. %) of Li_xSiON precursors dried at different temperatures in comparison with SP (60 °C/12 h/vacuum), analyzed by CasaXPS.

Compound	Condition	Li 1s	C 1s	N 1s	O 1s	Si 2p
SP	60 °C/12 h/vacuum	-	80.0	-	14.1	5.0
Li_2SiON	RT/1 h/vacuum	13.0	56.3	0.8	23.3	6.7
	60 °C/1 h/vacuum	12.9	55.5	0.8	24.3	6.5
	100 °C/1 h/vacuum	13.3	54.6	0.8	25.0	6.2
Li_4SiON	RT/1 h/vacuum	24.9	40.3	0.7	31.8	2.3
	60 °C/1 h/vacuum	23.9	42.8	1.0	28.0	4.2
	100 °C/1 h/vacuum	22.1	45.0	0.8	28.2	3.9
Li_6SiON	RT/1 h/vacuum	23.8	46.5	0.7	28.4	0.6
	60 °C/1 h/vacuum	25.2	46.0	0.9	27.2	0.7
	100 °C/1 h/vacuum	31.5	36.9	0.7	29.4	1.5

For the Li_6SiON precursor, C and O contents are similar to the Li_4SiON precursor, which may be related to the similar Li contents. However, after drying at 100 °C/1 h/vacuum, we can see a significant decrease in the C content and increases in the Li, O and Si contents. C may come from adsorbed organics during sample preparation that are volatile and removed on drying at a higher temperature resulting in increased percentages for the other elements.

However, the N content ranges between 0.7-0.9 at. % for all precursors. Since all samples were kept under vacuum overnight prior to XPS scans (10^{-9}-10^{-7} Torr), -NH_2 is like eliminated as NH_3, and the residual or "stable" N is similar for all precursors. In contrast, the MALDI studies on Li_xSiON solution droplets dried *in vacuo* for only a few minutes retained -NH_2 groups presenting much higher N contents (~5-30 at. % N excluding H) as suggested by composition calculations (Table **2**). It is also worth mentioning that the At. % analyzed by XPS may not be accurate as XPS only characterizes the sample surface to depths ≤10 nm.

Representative N 1s and Si 2p core-level XPS spectra of Li_xSiON precursors (dried at 60 °C/1 h/vacuum) are given in Figure **S13**. All Li_xSiON precursors show a N 1s peak at ~396-397 eV (Figure **S13a**), which can be ascribed to Li-**N**H from $LiNH_2$. Due to the low N content, the N 1s intensity is low for all precursors. It is noticeable that the N 1s peak shifts to lower binding energy (BE) as the Li content increases, i.e., BE of the N 1s peak (BE_N) follows Li_2SiON > Li_4SiON >

Li_6SiON, with a Δ_{BE} of 0.4-0.5 eV. Since the BE is related to electron density, as the electronegativity (EN) of surrounding atoms decreases, electron density increases for the base element and BE decreases. For Li_xSiON precursors, as the Li (low EN) content increases, Li^+ concentration increases but the "stable" N content stays at ~1 at. % for all precursors (Table **3**), resulting in increased electron density around N and thus lower BE.

For Si 2p XPS spectra, all Li_xSiON precursors exhibit Si $2p_{1/2}$ and $2p_{3/2}$ peaks ascribed to **Si-O** from SP. Similar to N 1s peaks, the Si 2p peak shifts to lower BE as the Li content increases (BE_{Si}: SP > Li_2SiON > Li_4SiON > Li_6SiON), which is likely due to the increased number of Li^+ that interact with the O from SP as suggested by NMR studies.

To study high temperature compositions of Li_xSiON precursors, precursor pellets (Figure **S3**) were heated to 800 °C/1 h/N_2 in a tube furnace and characterized by FTIR, XRD and XPS. Figure **S14a** compares the FTIRs of Li_xSiON heated to 800 °C/1 h/N_2. Peaks at ~1450 cm^{-1} are present for all precursors, which may be carbonate and/or silicate peaks. The peaks at ~1000-800 cm^{-1} are likely Si-O (~1050 cm^{-1}) and possibly some Si-N (960-840 cm^{-1}),[78–82] or silicate peaks.

Figure **S14b** compares the XRDs of Li_4SiON (800 °C/1 h/N_2) and Li_4SiO_4 as an example. Both the pellets and ground powder show the same diffraction peaks, suggesting phase uniformity of the bulk surface and interior. These peaks fit well with monoclinic Li_4SiO_4, in agreement with FTIR analyses in Figure **S14a**.

Figure **9a** compares the XPS spectra of Li_4SiON treated at RT/1 h/vacuum and 800 °C/1 h/N_2. Both spectra show the same main peaks for O, C, Si and Li. Only trace amounts of N are found in Li_4SiON treated at RT/1 h/vacuum, and no N in Li_4SiON treated at 800 °C/1 h/N_2.

Table **4** summarizes the XPS analyses of Li_4SiON treated at different temperatures. Li and O contents increase after heating to 800 °C while C and N contents decrease due to decomposition of organic groups.

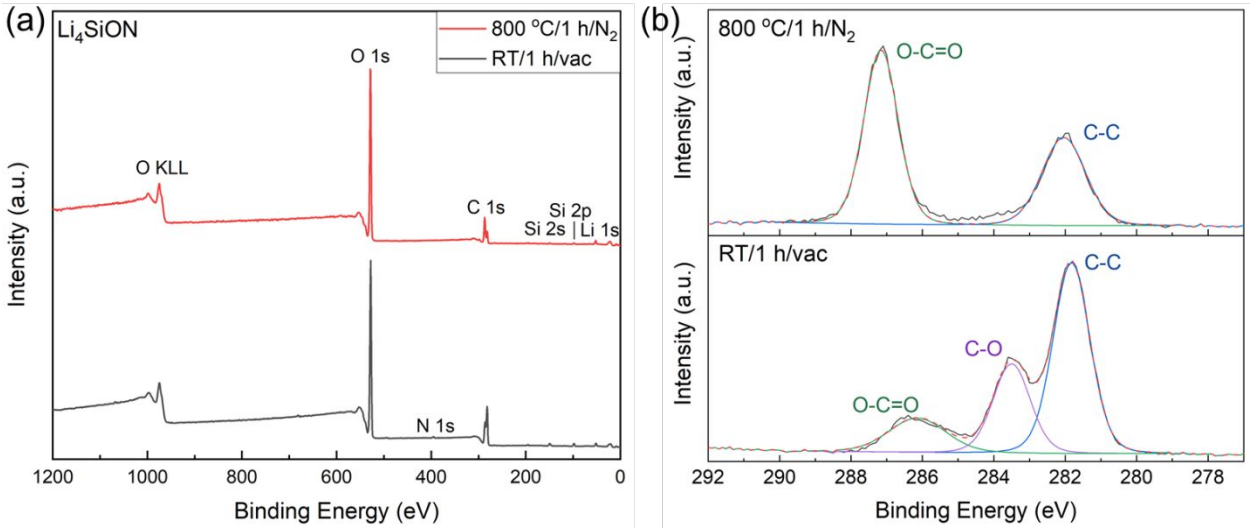

Figure **9a**. Wide-scan survey XPS spectra of Li_4SiON treated at RT/1 h/vacuum and 800 °C/1 h/N_2. **b**. C 1s core-level spectra of Li_4SiON treated at RT/1 h/vacuum and 800 °C/1 h/N_2.

Table 4. XPS analyses (by CasaXPS) of the Li_4SiON precursor treated at different temperatures.

	Condition	Li 1s	C 1s	N 1s	O 1s	Si 2p
Binding energy (eV)	RT/1 h/vacuum	52	282, 284, 286	396	529	99
	800 °C/1 h/N_2	52	282, 287	-	529	98
Average At. %	RT/1 h/vacuum	24.9	40.3	0.7	31.8	2.3
	800 °C/1 h/N_2	36.6	25.3	-	37.0	1.2

As for the binding energy, all elements remain mostly the same after heating to 800 °C except for C per Table **4**. Figure **9b** compares C 1s core-level spectra of Li_4SiON treated at RT/1 h/vacuum and 800 °C/1 h/N_2. The as-synthesized Li_4SiON (RT/1 h/vacuum) show three different C 1s peaks, corresponding to O-C=O from carbonate, and C-O and C-C from SP. After heating to 800 °C, as the organic components decompose, C-O disappears and the intensity of C-C drops (residual carbon), leaving a large carbonate peak (O-C=O) that also corresponds to the band at ~1450 cm^{-1} in the FTIR (Figure **S14a**). Overall, after heating to 800 °C/1 h/N_2, the precursors form stable crystalline Li_4SiO_4 and small amounts of Li_2CO_3.

To further characterize the composition and microstructures of the Li_xSiON precursors, SEM and EDX were conducted on precursor pellets (Figure **S3**), respectively.

Figure **10** shows SEM fracture surface images of Li_2SiON, Li_4SiON, and Li_6SiON precursor pellets heated to 100°-400 °C/2 h/N_2. The Li_4SiON and Li_6SiON pellets heated between 100°-200 °C, in general, showed a smooth, uniform, and dense microstructure, typical for polymeric materials. This can be ascribed to the fact that these precursors relatively show a small mass loss

(20 wt.%) before 250 °C. The densification at 200 °C for the Li_4SiON and Li_6SiON pellets might be a result of rearrangement between the polymeric chains during heat treatment, it may be also associated with a phase change as suggested by XRD for Li_6SiON (Figure **7c**). In comparison to pellets with high Li content, the microstructure of Li_2SiON pellet reveals porous structures on heating between 100°-200 °C, attributed to the large mass loss (50 wt.%) before 250 °C (Figure **6a**).

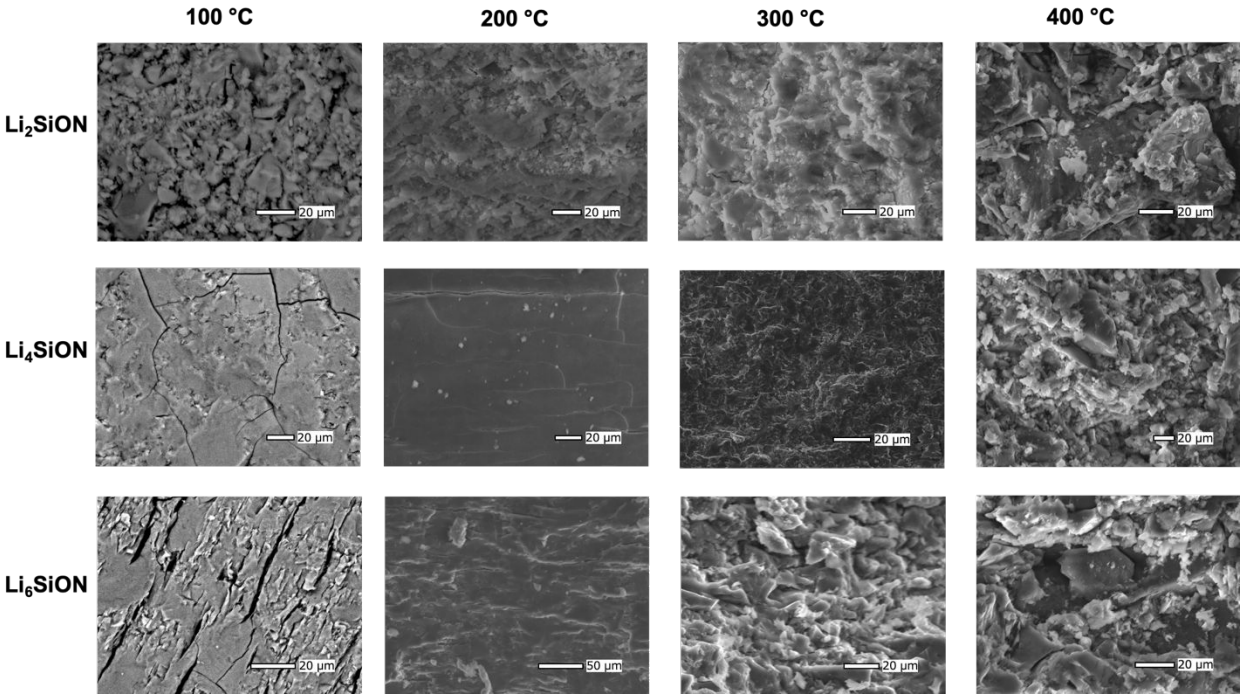

Figure 10. SEM fracture surface images of Li_xSiON pellets heated to 100°-400 °C/2 h/ N_2.

The pellets heated between 300°-400 °C exhibit crystalline features with uneven fracture surface (grain boundary fractures) as well as micro pores associated with the loss of volatile and organic compounds and ceramization of the precursors.

Table **S3** lists densities of Li_xSiON precursor pellets treated under different conditions. The as-synthesized precursors (dried at 60 °C/1 h/vacuum) show densities close to 1 g/cm^3, which is typical for polymeric materials. After heat treatment to 100°-400 °C/2 h/ N_2, all precursors show increased densities, which may be arised from polymeric structural rearrangements, and ceramization at higher temperatures (≥300 °C, Figure **10**). In general, the density increases with temperature, but Li_2SiON and Li_4SiON precursors show decreased density when the tempearture

increased from 300° to 400 °C, likely due to decomposition of organic compounds, consistent with SEM (Figure **10**) and TGA-DTA studies (Figure **6**). The Li_6SiON precursor shows better thermal stability as suggested by TGA-DTA (Figure **6**), therefore its density increases after heating to 400 °C.

Figures **S15-S17** show EDX map images of Li_xSiON pellets heated to 100°-400 °C/2 h/ N_2. The EDX map of pellets heated to 100 °C shows well-distributed signature elements (N, O, and Si) as well as C from the starting material (SP) in good agreement with XPS per Figure **8** and Table **3**. Quantitative EDX results are summarized in Table **S4**. In general, the N content decreases with increasing temperature. This is likely due to loss of $-NH_2$ (Table **3**). In addition, the C content also decreases as pellets are heated to 400 °C, also ascribed to decomposition of volatile and absorbed organic compounds (Figure **6**).

3.2. Ionic conductivity measurements

Figure **11** shows Nyquist plots of Li_2SiON, Li_4SiON, and Li_6SiON pellets heated to 100°-400 °C/2 h/N_2. All the measurements were conducted at room temperature. Detailed experimental procedures for ionic impedance measurements are provided in the SI.

Table **5** summarizes total conductivities of the polymer precursor pellets heated to 100°-400 °C/2 h/ N_2. The Li_2SiON pellet showed the highest conductivity when heated to 100 °C as shown in Figure **11a**. Conductivities decrease with increasing temperature to 300 °C, likely as a result of N loss per EDX in Figure **S15**. The slight increase in ionic conductivity at 400 °C for the Li_2SiON pellet might be a consequence of lower C contents. There seems to be a tradeoff between the loss of N and decreases in C content when the pellets are heated to higher temperatures (i.e. >300 °C) per Table **S4**. The decrease in C content is desirable as it decreases the electronic conductivity of the electrolyte.

Li_4SiON and Li_6SiON pellets show the highest conductivities of 9×10^{-7} and 8.5×10^{-6} S cm^{-1} at 200 °C, respectively. The increase in conductivity is associated with the denser microstructures of both precursors at 200 °C, Figure **10**. Conductivities then decrease on heating to 300°-400 °C, a likely result of the decrease in N contents.

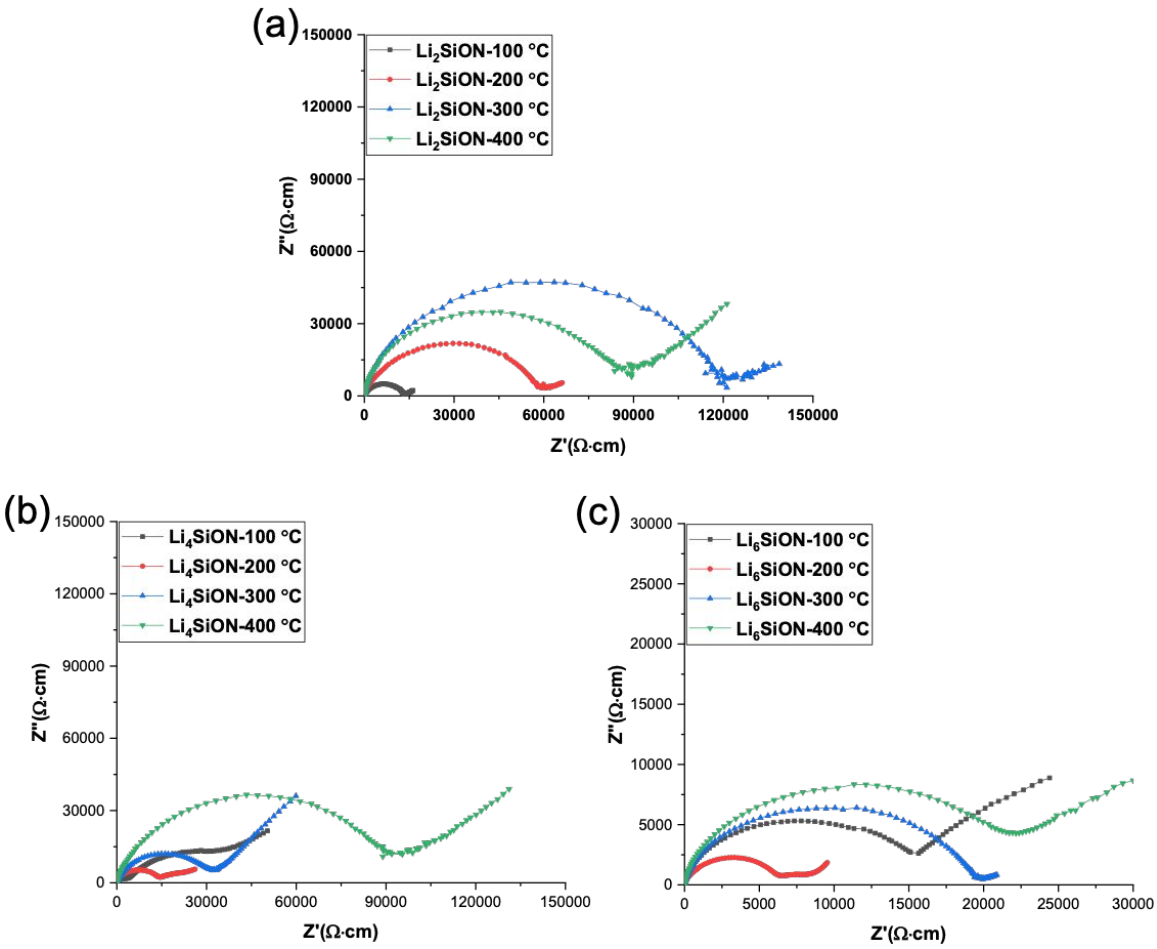

Figure 11. Nyquist plots of Li_xSiON pellets heated to 100°-400 °C/2 h/N_2.

Table 5. Total conductivities (σ_{RT}) of Li_xSiON pellets heated to 100°-400 °C/2 h/N_2.

Precursor pellet	Temp. (°C)	σ_{RT}(S cm^{-1})
Li_2SiON	100/2h	7.4×10^{-7}
	200/2h	2.5×10^{-7}
	300/2h	1.4×10^{-8}
	400/2h	2.0×10^{-8}
Li_4SiON	100/2h	2.3×10^{-7}
	200/2h	9.0×10^{-7}
	300/2h	4.6×10^{-7}
	400/2h	1.1×10^{-7}
Li_6SiON	100/2h	5.8×10^{-6}
	200/2h	8.5×10^{-6}
	300/2h	4.3×10^{-6}
	400/2h	2.7×10^{-6}

Table **6** compares the ionic conductivities of Li_4SiO_4 and LiSiON systems with different synthesis/processing methods in literature. Reported Li_4SiO_4 conductivities are typically measured at elevated temperatures (>100 °C). In general, Li_4SiO_4 sintered from sol-gel processed

nanopowders show higher conductivities compared to Li_4SiO_4 prepared via solid-state reaction. Adnan *et al*.[53] reported a high ambient bulk conductivity of ~3 × 10^{-6} S cm^{-1} for Li_4SiO_4 by sol-gel processing and sintering at 750 °C/4 h, which is still lower than the highest ambient conductivity of 8.5 × 10^{-6} S cm^{-1} for Li_6SiON heated to 200 °C/2 h. For N-doped systems, the only LiSiON glass ionic conductivity measurement found in the literature records a low value of 2.5 × 10^{-8} at 40 °C.[50]

Furthermore, compared to other synthesis and processing methods listed in Table **6**, the polymer precursor synthesis is easily scalable; dense microstructures (Figure **10**) and optimum conductivities (Table **5**) are obtained for Li_xSiON (x = 4, 6) pellets when heated only to 200 °C/2 h/N_2, which significantly reduces processing steps, temperatures, and cost.

Table 6. Comparison of ionic conductivities (σ) of Li_4SiO_4 and LiSiON systems with different synthesis/processing methods in the literature.

Composition/phase	Synthesis/processing method	σ (S cm^{-1}) at T °C	Thickness (mm)*	Ref.
Li_4SiO_4 (monoclinic)	Sol-gel and sintering (1000 °C/4 h)	~10^{-5} (250)	~2	51
Li_4SiO_4 (monoclinic)	Sol-gel and sintering (750 °C/4 h)	~3 × 10^{-6} (RT); ~10^{-4} (100)	-	53
Li_4SiO_4 (monoclinic)	Solid state reaction (1000-1050 °C/18-24 h)	~10^{-7} (150)	-	55,57
Li_4SiO_4 (monoclinic)	Solid state reaction (1200 °C/10 h)	2.5 × 10^{-6} (300)	-	59
$30Si_2O{\cdot}61SiO_2{\cdot}3Si_3N_4$ (LiSiON glass)	Melt mixing (1400-1450 °C/N_2)	2.5 × 10^{-8} (40)	~1	50
Li_6SiON (amorphous)	Polymer precursor synthesis and heating to 200 °C/2 h	8.5 × 10^{-6} (RT)	0.2-0.3	This work

*All conductivities are measured on pellets; thicknesses are not provided in some work.

Conclusions

In summary, we present here the green synthesis and detailed characterization of Li_xSiON oligomer/polymer precursors, including FTIR, MALDI-ToF, NMR, TGA-DTA, XRD, XPS, EDX, SEM and impedance studies. XPS shows that the Li content increases with $LiNH_2$ amounts, which also correlates with MWs and CYs. ^{7}Li NMR suggests that Li^+ ions are well solvated and dissociated, and excess Li^+ may exist in clusters, which is beneficial for their electrochemical performances. When x = 6, the Li content reaches a saturation level suggested by XPS; ^{1}H, ^{13}C and ^{29}Si NMRs indicate fluxional motion. Li_xSiON precursors start to decompose at ~100 °C due to organic portions. When dried at ≤100 °C, XRD patterns show amorphous phase; when heated

to 800 °C, Li_4SiO_4 forms, suggesting a polymer to ceramic conversion at higher temperatures. SEM and impedance studies show that dense microstructures and optimum conductivities are obtained after heating to 200 °C/2 h/N_2 for Li_xSiON (x = 4, 6) pellets. In general, conductivities of precursor pellets increase with Li content: Li_6SiON > Li_4SiON > Li_2SiON.

Future work will demonstrate the utility of these precursors, especially Li_6SiON when used in symmetric cells and half cells, impregnated in Celgard, or as solid solutions with PEO.

Acknowledgment

We are grateful for the support of a significant portion of this work by DMR NSF Grant No. DMR 1926199 and a gift from Mercedes Benz Research and Development North America (MBRDNA). A portion of the work was also supported by University of Michigan Rackham Merit fellowship. We also thank the University of Michigan Energy Institute (UMEI) and Michigan Translational Research and Commercialization (MTRAC) program for support of the purchase chemicals, solvents and furnace. We especially thank Mr. Andrew Alexander for his assistance in developing the computer program for polymer precursor composition calculations based on MALDI-ToF. We also thank Zejun Sun, Tianle Liu and Mengjie Yu for their help in synthesizing SP. We also would like to thank Wadham Energy LP for providing the RHA powders.

References

1 C. Yuan, H. B. Wu, Y. Xie and X. W. Lou, *Angew. Chem. Int. Ed.*, 2014, **53**, 1488–1504.
2 S. B. Peterson and J. J. Michalek, *Energy Policy*, 2013, **52**, 429–438.
3 L. L. Gaines and J. B. Dunn, in *Lithium-Ion Batteries*, ed. G. Pistoia, Elsevier, Amsterdam, 2014, pp. 483–508.
4 T. Jiang, P. He, G. Wang, Y. Shen, C.-W. Nan and L.-Z. Fan, *Adv. Energy Mater.*, 2020, **10**, 1903376.
5 A. Manthiram, X. Yu and S. Wang, *Nat. Rev. Mater.*, 2017, **2**, 1–16.
6 J. W. Fergus, *J. Power Sources*, 2010, **195**, 4554–4569.
7 K. Xu, *Chem. Rev.*, 2004, **104**, 4303–4418.
8 X.-B. Cheng, R. Zhang, C.-Z. Zhao, F. Wei, J.-G. Zhang and Q. Zhang, *Adv. Sci.*, 2016, **3**, 1500213.
9 C. S. Nimisha, K. Y. Rao, G. Venkatesh, G. M. Rao and N. Munichandraiah, *Thin Solid Films*, 2011, **519**, 3401–3406.
10 X. Yu, J. B. Bates, G. E. Jellison and F. X. Hart, *J. Electrochem. Soc.*, 1997, **144**, 524–532.
11 J. B. Bates, N. J. Dudney, G. R. Gruzalski, R. A. Zuhr, A. Choudhury, C. F. Luck and J. D. Robertson, *J. Power Sources*, 1993, **43–44**, 103–110.
12 A. Reyes Jiménez, R. Nölle, R. Wagner, J. Hüsker, M. Kolek, R. Schmuch, M. Winter and T. Placke, *Nanoscale*, 2018, **10**, 2128–2137.

13 Z. Hu, D. Li and K. Xie, *Bull. Mater. Sci.*, 2008, **31**, 681–686.
14 S. J. Lee, J. H. Bae, H. W. Lee, H. K. Baik and S. M. Lee, *J. Power Sources*, 2003, **123**, 61–64.
15 F. Muñoz, A. Durán, L. Pascual, L. Montagne, B. Revel and A. C. M. Rodrigues, *Solid State Ion.*, 2008, **179**, 574–579.
16 P. E. Stallworth, F. Vereda, S. G. Greenbaum, T. E. Haas, P. Zerigian and R. B. Goldner, *J. Electrochem. Soc.*, 2005, **152**, A516–A522.
17 B. Fleutot, B. Pecquenard, H. Martinez, M. Letellier and A. Levasseur, *Solid State Ion.*, 2011, **186**, 29–36.
18 N. Mascaraque, J. L. G. Fierro, A. Durán and F. Muñoz, *Solid State Ion.*, 2013, **233**, 73–79.
19 J. B. Bates, N. J. Dudney, G. R. Gruzalski, R. A. Zuhr, A. Choudhury, C. F. Luck and J. D. Robertson, *Solid State Ion.*, 1992, **53**, 647–654.
20 B. Wang, B. S. Kwak, B. C. Sales and J. B. Bates, *J. Non-Cryst. Solids*, 1995, **183**, 297–306.
21 B. Put, P. M. Vereecken, J. Meersschaut, A. Sepúlveda and A. Stesmans, *ACS Appl. Mater. Interfaces*, 2016, **8**, 7060–7069.
22 Y. Hamon, A. Douard, F. Sabary, C. Marcel, P. Vinatier, B. Pecquenard and A. Levasseur, *Solid State Ion.*, 2006, **177**, 257–261.
23 S. Zhao, Z. Fu and Q. Qin, *Thin Solid Films*, 2002, **415**, 108–113.
24 W. Y. Liu, Z. W. Fu, C. L. Li and Q. Z. Qin, *Electrochem. Solid-State Lett.*, 2004, **7**, J36–J40.
25 F. Vereda, R. B. Goldner, T. E. Haas and P. Zerigian, *Electrochem. Solid-State Lett.*, 2002, **5**, 239–241.
26 Y. G. Kim and H. N. G. Wadley, *J. Vac. Sci. Technol. Vac. Surf. Films*, 2008, **26**, 174–183.
27 S. Nowak, F. Berkemeier and G. Schmitz, *J. Power Sources*, 2015, **275**, 144–150.
28 H. T. Kim, T. Mun, C. Park, S. W. Jin and H. Y. Park, *J. Power Sources*, 2013, **244**, 641–645.
29 F. Xu, N. J. Dudney, G. M. Veith, Y. Kim, C. Erdonmez, W. Lai and Y. M. Chiang, *J. Mater. Res.*, 2010, **25**, 1507–1515.
30 A. C. Kozen, A. J. Pearse, C. F. Lin, M. Noked and G. W. Rubloff, *Chem. Mater.*, 2015, **27**, 5324–5331.
31 B. Wang, B. C. Chakoumakos, B. C. Sales, B. S. Kwak and J. B. Bates, *J. Solid State Chem.*, 1995, **115**, 313–323.
32 N. S. Roh, S. D. Lee and H. S. Kwon, *Scr. Mater.*, 1999, **42**, 43–49.
33 L. Meda and E. E. Maxie, *Thin Solid Films*, 2012, **520**, 1799–1803.
34 L. Le Van-Jodin, F. Ducroquet, F. Sabary and I. Chevalier, *Solid State Ion.*, 2013, **253**, 151–156.
35 Y. Su, J. Falgenhauer, A. Polity, T. Leichtweiß, A. Kronenberger, J. Obel, S. Zhou, D. Schlettwein, J. Janek and B. K. Meyer, *Solid State Ion.*, 2015, **282**, 63–69.
36 P. Birke, W. F. Chu and W. Weppner, *Solid State Ion.*, 1996, **93**, 1–15.
37 P. Birke and W. Weppner, *Electrochimica Acta*, 1997, **42**, 3375–3384.
38 Y. Hamon, P. Vinatier, E. I. Kamitsos, M. Dussauze, C. P. E. Varsamis, D. Zielniok, C. Roesser and B. Roling, *Solid State Ion.*, 2008, **179**, 1223–1226.
39 M. Dussauze, E. I. Kamitsos, P. Johansson, A. Matic, C. P. E. Varsamis, D. Cavagnat, P. Vinatier and Y. Hamon, *J. Phys. Chem. C*, 2013, **117**, 7202–7213.
40 K. H. Joo, H. J. Sohn, P. Vinatier, B. Pecquenard and A. Levasseur, *Electrochem. Solid-State Lett.*, 2004, **7**, 256–259.
41 W. Yang, W. Yang, B. Sun, S. Di, K. Yan, G. Wang and G. Shao, *ACS Appl. Mater. Interfaces*, 2018, **10**, 39695–39704.

42 B. Dong, R. Jarkaneh, S. Hull, N. Reeves-McLaren, J. J. Biendicho and A. R. West, *J. Mater. Chem. A*, 2015, **4**, 1408–1413.
43 R. Jarkaneh, Novel Oxynitride Lithium Ion Conductors, 2015.
44 H. Unuma, *J. Am. Ceram. Soc.*, 1993, **76**, 1308–1312.
45 H. Unuma, T. Kokubo and S. Sakka, *J. Mater. Sci.*, 1988, **23**, 4399–4405.
46 N. A. Wójcik, B. Jonson, D. Möncke, E. I. Kamitsos, H. Segawa, J. Karczewski and S. Ali, *J. Non-Cryst. Solids*, 2019, **522**, 119585.
47 S. Sakka, *J. Non-Cryst. Solids*, 1995, **181**, 215–224.
48 H. Unuma, Y. Suzuki, T. Furusaki, Y. Ishizuka and K. Kodaira, *J. Ceram. Soc. Jpn.*, 1989, **97**, 376–379.
49 H. Unuma and S. Sakka, *J. Mater. Sci. Lett.*, 1987, **6**, 996–998.
50 H. Unuma, K. Komori and S. Sakka, *J. Non-Cryst. Solids*, 1987, **95**, 913–920.
51 X. Wu, Z. Wen, X. Xu, X. Wang and J. Lin, *J. Nucl. Mater.*, 2009, **392**, 471–475.
52 X. Wu, Z. Wen, X. Xu and Y. Liu, *Fusion Eng. Des.*, 2010, **85**, 222–226.
53 S. B. R. S. Adnan, N. S. Mohamed and K. A. Norwati, *Int. J. Eng. Math. Phys. Sci.*, 2011, **5**, 183–186.
54 A. R. West, *J. Appl. Electrochem.*, 1973, **3**, 327–335.
55 A. Khorassani and A. R. West, *J. Solid State Chem.*, 1984, **53**, 369–375.
56 Y. Tao, D. Yi and J. Li, *Solid State Ion.*, 2008, **179**, 2396–2398.
57 A. Khorassani and A. R. West, *Solid State Ion.*, 1982, **7**, 1–8.
58 Y. Sakurai, A. Sakuda, A. Hayashi and M. Tatsumisago, *Solid State Ion.*, 2011, **182**, 59–63.
59 Y. Deng, C. Eames, J. N. Chotard, F. Laleìre, V. Seznec, S. Emge, O. Pecher, C. P. Grey, C. Masquelier and M. S. Islam, *J. Am. Chem. Soc.*, 2015, **137**, 9136–9145.
60 K. Hirai, M. Tatsumisago and T. Minami, *Solid State Ion.*, 1995, **78**, 269–273.
61 Y. Kawakami, H. Ikuta, T. Uchida and M. Wakihara, *Thermochim. Acta*, 1997, **299**, 7–12.
62 H. Morimoto, H. Yamashita, M. Tatsumisago and T. Minami, *J. Ceram. Soc. Jpn.*, 2000, **108**, 128–131.
63 M. Tatsumisago, H. Morimoto, H. Yamashita and T. Minami, *Solid State Ion.*, 2000, **136–137**, 483–488.
64 Y. Ikeda, T. Kitade, S. Kohjiya, A. Hayashi, A. Matsuda, M. Tatsumisago and T. Minami, *Polymer*, 2001, **42**, 7225–7228.
65 X. Zhang, E. Temeche and R. M. Laine, *Macromolecules*, 2020, **53**, 2702–2712.
66 E. Temeche, X. Zhang and R. M. Laine, *ACS Appl. Mater. Interfaces*, 2020, **12**, 20548–20562.
67 E. Temeche, X. Zhang and R. M. Laine, *ACS Appl. Mater. Interfaces*, 2020, **12**, 30353–30364.
68 E. Temeche, M. Yu and R. M. Laine, *Green Chem.*, 2020, **22**, 4656–4668.
69 J. C. Marchal, D. J. Krug, P. McDonnell, K. Sun and R. M. Laine, *Green Chem.*, 2015, **17**, 3931–3940.
70 R. M. Laine, J. C. Furgal, P. Doan, D. Pan, V. Popova and X. Zhang, *Angew. Chem. - Int. Ed.*, 2016, **55**, 1065–1069.
71 J. C. Furgal and R. M. Laine, *Bull. Chem. Soc. Jpn.*, 2016, **89**, 705–725.
72 M. L. Hoppe, R. M. Laine, J. Kampf, M. S. Gordon and L. W. Burggraf, *Angew. Chem. Int. Ed. Engl.*, 1993, **32**, 287–289.
73 F. A. Cotton, *Acc. Chem. Res.*, 1968, **1**, 257–265.
74 P. I. Arvidsson, P. Ahlberg and G. Hilmersson, *Chem. - Eur. J.*, 1999, **5**, 1348–1354.
75 K. K. Lee, K. Park, H. Lee, Y. Noh, D. Kossowska, K. Kwak and M. Cho, *Nat. Commun.*, 2017, **8**, 1–9.

76 K. A. See, M. Leskes, J. M. Griffin, S. Britto, P. D. Matthews, A. Emly, A. Van Der Ven, D. S. Wright, A. J. Morris, C. P. Grey and R. Seshadri, *J. Am. Chem. Soc.*, 2014, **136**, 16368–16377.
77 J. Zhang and Y. H. Hu, *Ind. Eng. Chem. Res.*, 2011, **50**, 8058–8064.
78 G. Scardera, T. Puzzer, G. Conibeer and M. A. Green, *J. Appl. Phys.*, 2008, **104**, 104310.
79 E. San Andrés, A. Del Prado, F. L. Martínez, I. Mártil, D. Bravo and F. J. López, *J. Appl. Phys.*, 2000, **87**, 1187–1192.
80 J. A. Diniz, P. J. Tatsch and M. A. A. Pudenzi, *Appl. Phys. Lett.*, 1996, **69**, 2214–2215.
81 H. Ono, T. Ikarashi, Y. Miura, E. Hasegawa, K. Ando and T. Kitano, *Appl. Phys. Lett.*, 1999, **74**, 203–205.
82 J. Viard, E. Beche, D. Perarnau, R. Berjoan and J. Durand, *J. Eur. Ceram. Soc.*, 1997, **17**, 2025–2028.